Chemical Science

ROYAL SOCIETY OF CHEMISTRY

EDGE ARTICLE

View Article Online
View Journal | View Issue

Cite this: *Chem. Sci.*, 2026, **17**, 7667

All publication charges for this article have been paid for by the Royal Society of Chemistry

Tuning the electronic structure of molybdenum oxide nanoclusters with vanadium doping for electrochemical H_2O_2 production

Luyao Zhang,†[a] Yingbo Li,†[a] Shuhao Zhang,[b] Jianghua Wu,[a] Weiyang Xue,[a] Kun Wang,[a] Haojie Liu,[a] Boyuan Yu,[a] Xin Zhao,[a] Jiangfeng Ni*[b] and Feng Yang*[a]

Received 13th September 2025
Accepted 17th February 2026

DOI: 10.1039/d5sc07071f

rsc.li/chemical-science

Electrosynthesis of H_2O_2 has gained tremendous attention as a highly promising alternative strategy to the traditional anthraquinone technique. Nevertheless, there is still a lack of highly efficient, robust, and low-cost electrocatalysts to propel the industrialization of electrosynthesis of H_2O_2. Herein, we constructed carboxyl functionalized CNTs decorated with V-doped MoO_x nanoclusters ($MoVO_x$ NCs/CNTs) with uniform subnanometer size (~0.7 nm). The incorporation of V significantly modified the electronic structure of MoO_x, enabling an impressive H_2O_2 electrosynthesis selectivity of up to 98% at 0.4 V, surpassing that of the undoped MoO_x NCs/CNTs. The $MoVO_x$ NCs/CNTs catalyst retained 93% H_2O_2 electrosynthesis selectivity across a wide potential range (0.2–0.6 V). Moreover, the catalyst demonstrated excellent activity stability for 10 h with minimal decay. This work offers a pathway by rational design of a subnanometer catalyst for the electrocatalysis of O_2 to H_2O_2.

Introduction

Since its first discovery by Thenard in 1818, hydrogen peroxide (H_2O_2) has been regarded as one of the 100 most important chemicals and found wide application in various areas, including paper bleaching, pharmaceutical synthesis, and wastewater degradation.[1–8] Impressively, it was estimated that the global quantity demand of H_2O_2 would reach 6.0 million metric tons in 2024.[9,10] Currently, over 95% of H_2O_2 stock solutions (~30–70 wt%) strongly rely on the well-established anthraquinone oxidation process.[11,12] It is an energy-intensive technique, involving sequential hydrogenation/autoxidation of 2-alkyl-9/10-anthraquinone under high pressure with the aid of expensive Pd/Ni catalysts, followed by complicated purification procedures.[2,13–15] Consequently, the tremendous industrial waste generated and the high risk of storage/transportation remarkably deviate from our pursuit of green chemistry.[16,17] Moreover, most applications typically require low concentrations of H_2O_2.

Recently, with the rapid development of nanosized catalysts, electrosynthesis of H_2O_2 through a $2e^-$ oxygen reduction reaction (ORR) pathway ($O_2 + 2H_2O + 2e^- \rightarrow H_2O_2 + 2OH^-$) ($U^0 = 0.76$ V *vs.* RHE, where RHE represents the reversible hydrogen electrode) has emerged as a highly appealing alternative strategy.[5,14,18] Compared with the anthraquinone process, the electrochemical approach holds several advantages, including mild production conditions in ordinary atmospheric environments, suitability for on-site/on-demand production to avoid the risk of storage/transportation, environmental friendliness and organic waste emission, and the avoidance of explosive hazards by spatially separating H_2 and O_2 feeding.[2,19–22] However, it is worth noting that the ORR also involves another thermodynamically favourable $4e^-$ pathway that converts O_2 to H_2O ($O_2 + 2H_2O + 4e^- \rightarrow 4OH^-$) ($U^0 = 0.40$ V *vs.* RHE) which inevitably suppresses H_2O_2 production.[23,24] Accordingly, one major challenge for electrosynthesis of H_2O_2 is to find an efficient and robust electrocatalyst with high selectivity towards the $2e^-$ ORR.

Mechanistically, the ORR selectivity is highly dependent on the adsorption strength between the *OOH intermediate and the surface of catalysts.[4,25] In detail, an intensive interaction could easily dissociate the O–O bond and induce the $4e^-$ ORR, while too-weak cooperation may require a high overpotential to trigger the reaction.[26] Therefore, the appropriate interaction strength is a critical knob for designing efficient $2e^-$ ORR catalysts. Therefore, a great variety of catalysts have been developed, ranging from noble metals (Au–Pd),[27] metal chalcogenides ($CoSe_2$),[7] conducting coordination compounds (cobalt–porphyrins),[28] and carbon-based materials (N-doped oxo-functionalized graphene).[29] In particular, metal-free carbonaceous materials have garnered tremendous attention due to their abundance, low cost, and high selectivity for the $2e^-$ ORR.[9,30,31] For instance, Lu *et al.* demonstrated that the as-

[a]*Department of Chemistry, Southern University of Science and Technology, Shenzhen, 518055, China. E-mail: yangf3@sustech.edu.cn*

[b]*School of Physical Science and Technology, Center for Energy Conversion Materials & Physics (CECMP), Jiangsu Key Laboratory of Thin Films, Soochow University, Suzhou 215006, China. E-mail: jeffni@suda.edu.cn*

† These authors contributed equally.

prepared oxidized carbon nanotubes (CNTs) exhibited high activity for the $2e^-$ ORR and claimed that the responsible active sites were the carbon atoms adjacent to carboxylic acid and other oxo-functional groups.[32] Targeting further improving the performance of metal-free carbonaceous materials, introducing isolated metal single atoms into a carbon matrix to form single-atom catalysts (SACs) exhibits profound potential application in electrosynthesis of H_2O_2.[33–38] Despite substantial progress, the catalyst design and the properties still need further revolutionization to meet the high criterion of practical application.

Nanocluster catalysts (M_x, where M and x refer to the metal and atom number, respectively) play a pivotal role in bridging the gap between SACs and nanoparticles. They not only share similar characteristics with SACs, such as maximized metal atom utilization and well-defined active sites, but also offer additional catalytic sites with adjacent metal atoms.[33,39–41] As compared to M_x–N_y and M_x–C_y coordination structures, the highly electronegative O atom could induce accelerated electron transfer from M_x to O_y, potentially resulting in a favourable energy band structure and unexpected catalytic activity.[42] Additionally, as a 4d transition metal, Mo possesses more intricate oxidation states and coordination numbers and has received less attention compared to the well-reported 3d transition metals (Fe, Co, Ni, *etc.*).[43] On the other hand, polyoxometalates (POMs) are a type of well-defined anionic oxo–metal cluster with unique redox properties.[44] Their charge density and coordination structures can be precisely tailored by adjusting their composition.[45] As a typical POM, the above-mentioned characteristics make $H_3PMo_{12}O_{40}$ an ideal precursor for constructing MoO_x nanoclusters. Besides, doping a metal (*e.g.*, V) with a lower d-orbital occupancy and electronegativity into MoO_x nanoclusters may further optimize their electronic structure[46–48] for reaction intermediate adsorption/desorption and stimulate the catalytic activity.

Herein, we prepared carboxyl functionalized CNTs decorated with vanadium-doped MoO_x nanoclusters ($MoVO_x$ NCs/CNTs) through a mild thermal treatment using V-substituted $H_3PMo_{12}O_{40}$ ($H_6PMo_9V_3O_{40}$) as a precursor. The $MoVO_x$ NCs were not only supported on the surface of CNTs, but also confined within the cavities of CNTs. Based on the advanced spectroscopic techniques, it was found that the doping of V could reduce the valence state of Mo in $MoVO_x$ NCs/CNTs, enabling Mo with a higher electronic cloud density, and thereby significantly modify the electronic structure of MoO_x NCs. Consequently, $MoVO_x$ NCs/CNTs exhibit an impressive $2e^-$ ORR selectivity of up to 98% at 0.4 V in 0.1 M KOH solution, which far exceeds that of their counterpart MoO_x NCs/CNTs. Notably, $MoVO_x$ NCs/CNTs could retain more than 93% $2e^-$ ORR selectivity in a wide potential range (0.2–0.6 V). Furthermore, $MoVO_x$ NCs/CNTs demonstrated excellent activity stability for 10 h with negligible decay.

Results and discussion

Preparation and characterization of $MoVO_x$ NCs/CNTs

V-substituted $H_3PMo_{12}O_{40}$ ($H_6PMo_9V_3O_{40}$) was synthesized according to the literature. Within a POM unit, there are four distinct types of oxygen atoms: central oxygen (O_c), terminal oxygen (O_t), bridged oxygen between two octahedra sharing a corner (O_b), and bridged oxygen that shares an edge (O_e). Intense bands at 1058, 955, 881, and 768 cm^{-1} can be observed in the Fourier-transform infrared spectra (Fig. S1) of $H_3PMo_{12}O_{40}$ and $H_6PMo_9V_3O_{40}$, corresponding to the vibrations of P–O_c, Mo–O_t, Mo–O_b–Mo, and Mo–O_e–Mo, respectively.[49] These results confirm the formation of $H_6PMo_9V_3O_{40}$. Notably, the phenomenon of blue shift, characterized by a migration towards higher wavenumbers in $H_6PMo_9V_3O_{40}$, typically signifies alterations in the vibrational frequencies of chemical bonds or functional groups within a molecule. Such shifts may arise from the strengthening of chemical bonds, modifications in the intramolecular charge distribution, and intermolecular interactions after the doping of V.

The synthesis procedures of MoO_x NCs/CNTs and $MoVO_x$ NCs/CNTs are schematically displayed in Fig. S2. $H_3PMo_{12}O_{40}$ or $H_6PMo_9V_3O_{40}$ and carboxyl functionalized CNTs were mixed and self-assembled by magnetic stirring for 48 h. The resultant powders were then subjected to a heat treatment at 500 °C for 30 min under a 10% H_2/Ar atmosphere through a rapid heating-cooling strategy. During this process, $H_3PMo_{12}O_{40}$ and $H_6PMo_9V_3O_{40}$ underwent thermal decomposition and reduction and were converted to MoO_x and $MoVO_x$ nanoclusters, respectively. The morphology of the as-prepared MoO_x NCs/CNTs and $MoVO_x$ NCs/CNTs was revealed by transmission electron microscopy (TEM). The high-angle annular dark-field scanning TEM (HAADF-STEM) images clearly demonstrated the presence of tiny nanoclusters both on outer walls and inner cavities of CNTs (Fig. 1a and S3a). The corresponding STEM-energy dispersive X-ray (EDX) elemental mapping further proved that the Mo, O, and V elements were uniformly distributed throughout CNTs, indicating the bright dots consisted of Mo, O, and V (Fig. 1b and S3b).

To further elucidate the structure of these clusters, aberration-corrected STEM was conducted. The subnanometer clusters in $MoVO_x$ NCs/CNTs and MoO_x NCs/CNTs were identified to be composed of Mo/V atoms with an average diameter of 0.67 nm and 0.75 nm, respectively (Fig. 1c–e and S3c, d). More aberration-corrected STEM images of $MoVO_x$ NCs/CNTs are shown in Fig. S4. The powder X-ray diffraction (XRD) patterns showed that instead of yielding sharp diffraction peaks, the phenomenon manifests as broad, diffuse background signals, implying the amorphous structure of tiny clusters in both $MoVO_x$ NCs/CNTs and MoO_x NCs/CNTs (Fig. 1f). Moreover, no diffraction peaks can be ascribed to the characteristics of crystalized MoO_2 or MoO_3.

Electrocatalytic ORR activities towards H_2O_2

The electrocatalytic performance of the as-prepared hybrid catalysts for the $2e^-$ ORR was evaluated using the typical rotating ring-disk electrode (RRDE) equipment, with an optimized catalyst loading of 0.1 mg cm^{-2}. All potential reported in this work is calibrated to RHE (Fig. S5). Fig. 2a shows the linear sweep voltammetry (LSV) curves collected at 1600 rpm in O_2-saturated 0.1 M KOH electrolyte, together with the H_2O_2

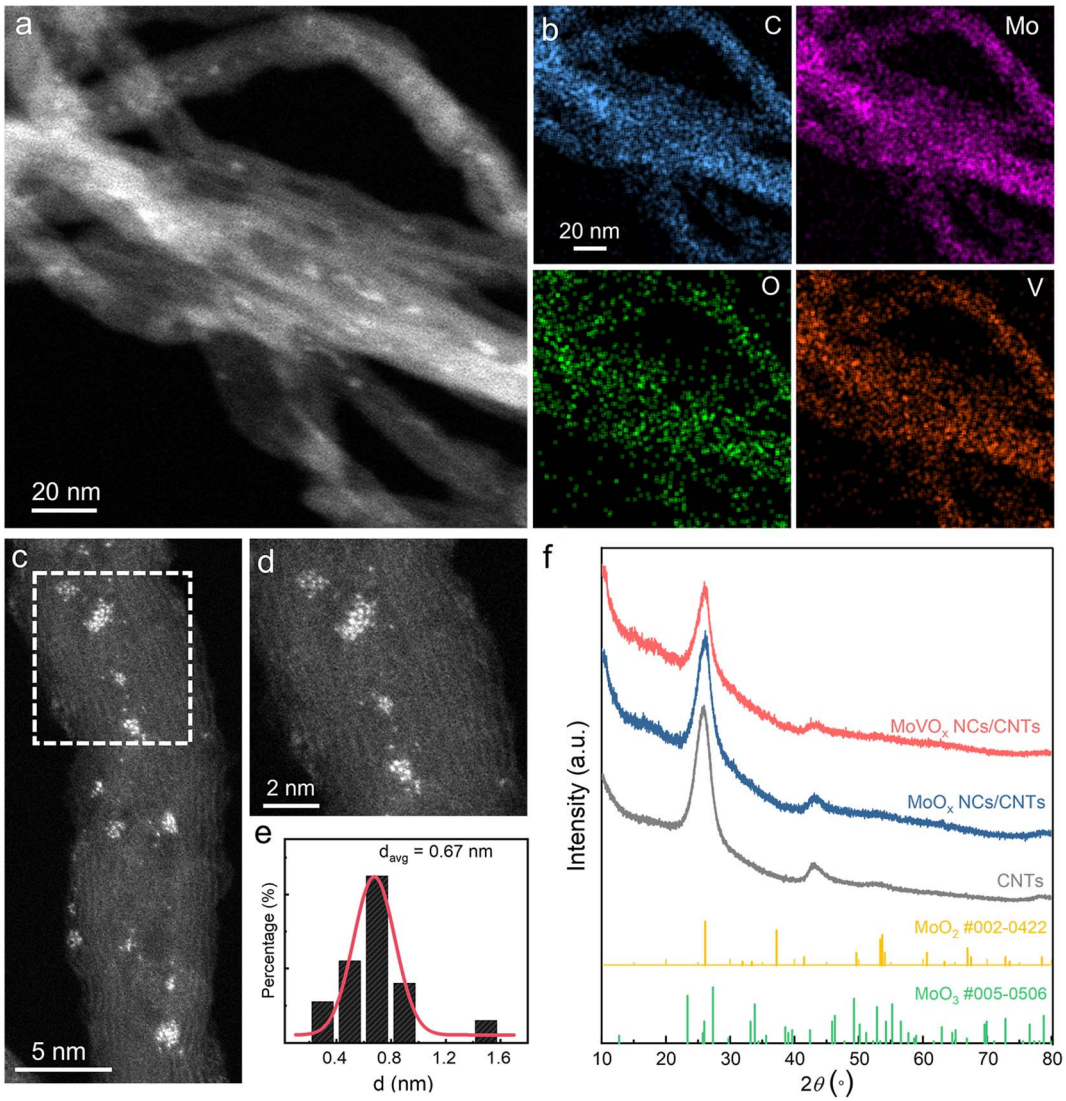

Fig. 1 Characterization of $MoVO_x$ NCs/CNTs. (a) and (b) HAADF-STEM image and the corresponding STEM-EDX elemental mapping of $MoVO_x$ NCs/CNTs. (c) and (d) High-resolution HAADF-STEM images, and (e) the corresponding cluster size distribution. (f) XRD patterns of CNTs, MoO_x NCs/CNTs and $MoVO_x$ NCs/CNTs. The standard cards of MoO_2 and MoO_3 are also shown.

oxidation current collected using the Pt ring electrode at a constant potential of 1.2 V *versus* RHE. The $MoVO_x$ NCs/CNTs exhibit the highest ring current (up to 210 μA), which is substantially greater than that of MoO_x NCs/CNTs and the CNTs benchmark. Additionally, there is only a minimal difference in disk current observed for all three samples. These findings indicate that $MoVO_x$ NCs/CNTs possess the highest $2e^-$ ORR selectivity among the tested catalysts, making them capable of achieving the highest H_2O_2 yield.

To accurately assess the selectivity for H_2O_2 production, the collection efficiency (N) of the RRDE was first calibrated using the redox reactions of potassium ferricyanide (Fig. S6). The experimentally determined collection efficiency is 34.2%, which was then used to calculate the selectivity for H_2O_2 production and the number of electrons transferred during the ORR. The calculated H_2O_2 selectivity and electron transfer number (n) were plotted as a function of potential (Fig. 2b). In the wide potential range of 0.2–0.6 V, the H_2O_2 selectivity of $MoVO_x$ NCs/CNTs consistently remained above 93%, indicating the highly selective $2e^-$ ORR pathway. Notably, the selectivity further increased to 98% at 0.4 V *vs.* RHE. Moreover, the calculated electron transfer number was less than 2.2, further confirming the dominance of the $2e^-$ ORR pathway during the ORR process. On the other hand, MoO_x NCs/CNTs exhibited a lower H_2O_2 selectivity of ~80% with a higher electron transfer number, indicating the critical role of V in promoting H_2O_2 generation. Additionally, the Tafel plots derived from LSV curves were obtained to examine the kinetic reaction rate. The Tafel slope of $MoVO_x$ NCs/CNTs (59.7 mV dec^{-1}) is noticeably lower than that of MoO_x NCs/CNTs (65.8 mV dec^{-1}) and CNTs (78.6 mV dec^{-1}), implying that $MoVO_x$ NCs/CNTs hold the best kinetic reaction rate (Fig. 2c). These results highlight the superior electrocatalysis performance of $MoVO_x$ NCs/CNTs in terms of electrosynthesis of H_2O_2.

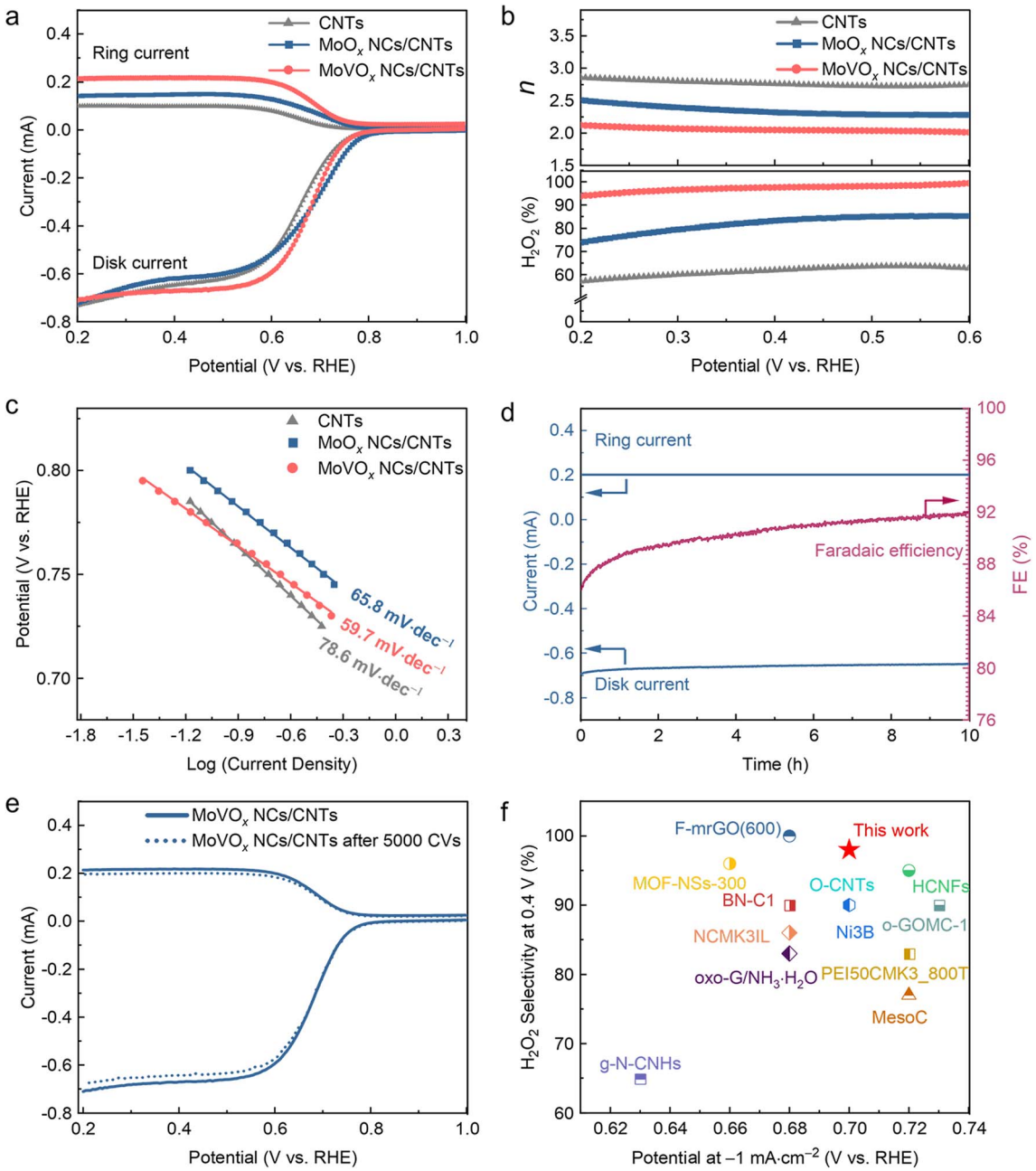

Fig. 2 2e$^-$ ORR performance of MoVO$_x$ NCs/CNTs in 0.1 M KOH. (a) Disk and ring current of the three samples on the RRDE. (b) The corresponding electron transfer number n and H_2O_2 selection at various potentials. (c) The corresponding Tafel plots. (d) Stability measurement of MoVO$_x$ NCs/CNTs at a fixed disk potential of 0.4 V *vs.* RHE and the corresponding faradaic efficiency. (e) ORR LSV curves of MoVO$_x$ NCs/CNTs before and after 5000 ADT cycles. (f) Performance comparison of electrochemical H_2O_2 production in alkaline media on MoVO$_x$ NCs/CNTs and other recently reported catalysts based on RRDE performance.

Stability is another key indicator to assess the performance of catalysts for electrosynthesis of H_2O_2. We conducted a long-term stability test for MoVO$_x$ NCs/CNTs using a chronoamperometric test at a constant disk potential of 0.4 V *vs.* RHE. The H_2O_2 selectivity remained consistently around 98% with negligible fluctuation during the 10 h continuous operation (Fig. 2d), suggesting the robust electrocatalytic stability for the 2e$^-$ ORR. In addition, we also performed an accelerated degradation test (ADT) to further demonstrate the robust stability of MoVO$_x$ NCs/CNTs. The obtained LSV curves before and after the 5000 ADT cycles were essentially identical (Fig. 2e), confirming the impressive cycling stability of MoVO$_x$ NCs/CNTs. Specifically, MoVO$_x$ NCs/CNTs afforded an outstanding H_2O_2 selectivity of ~98% at a current density of 1.0 mA cm^{-2}, surpassing that of previously reported electrocatalysts (Fig. 2f and Table S1). RRDE measurements are highly reproducible across three independently prepared batches, with relative standard deviations below 5% (Fig. S7). Since catalyst durability is closely tied to structural and compositional integrity, we carried out comprehensive post-stability characterization

studies to assess possible changes and to better understand the long-term performance. The electronic structure of $MoVO_x$ NCs/CNTs remains largely intact after electrochemical testing, with negligible alterations (Fig. S8a). We further tested the leaching amount of V during the stability test. We regularly monitored the V ion content in solution by inductively coupled plasma mass spectrometry (ICP-MS). The results show only 1.4% of V leaching after a 10 h long-term stability test, confirming that V leaching during electrochemical operation can be safely excluded (Fig. S8b). All the results indicated that $MoVO_x$ NCs/CNTs hold great promise as a highly efficient and robust $2e^-$ ORR electrocatalyst in alkaline media.

It has been demonstrated that metal-free carbonaceous materials with abundant oxo-functional groups are promising, efficient $2e^-$ ORR electrocatalysts in alkaline media.[5,9,23,32] Given the reported activity of strongly oxidized CNTs for the $2e^-$ ORR, we prepared further deep-oxidized CNTs as a control sample by refluxing blank carboxylated CNTs in concentrated HNO_3 at 140 °C for 2.5 h following literature procedures.[50] The normalized XPS survey spectra show a pronounced increase in the O 1s signal after oxidation (Fig. S9), with the oxygen content increasing from 7.7% for the blank carboxylated CNTs to 19.1% for the deep-oxidized CNTs, indicating a substantially more oxygen-rich CNT surface. Under identical electrode preparation and RRDE testing conditions, deep-oxidized CNTs deliver an H_2O_2 selectivity of ~70% at 0.4 V in 0.1 M KOH, slightly higher than that of blank carboxylated CNTs support (~60%) but still substantially lower than that of $MoVO_x$ NCs/CNTs (98%) (Fig. S10). These results suggest that increasing surface oxygen content can improve H_2O_2 selectivity to a limited extent. However, oxygen enrichment alone cannot account for the near-quantitative selectivity, supporting that the $MoVO_x$ nanoclusters play a key role in enabling highly selective $2e^-$ ORR.

To evaluate the applicability of the $MoVO_x$ NCs/CNTs catalyst under more challenging acidic conditions, we further performed ORR measurements in an O_2-saturated in 0.05 M H_2SO_4 at 1600 rpm. CNTs, MoO_x NCs/CNTs, and $MoVO_x$ NCs/CNTs all remain ORR-active in acid and deliver measurable H_2O_2 production, evidenced by the resolved disk and ring current responses (Fig. S11). Compared with alkaline media, the reaction kinetics in acidic electrolyte are noticeably slower, as reflected by larger Tafel slopes and substantially reduced H_2O_2-related ring currents, which is consistent with the commonly observed limitations of non-precious-metal, carbon-based catalysts in acidic environments, where stronger proton adsorption, reduced site stability, and intensified competition from the $4e^-$ ORR pathway often constrain performance.[51,52] Notably, under identical testing conditions, the V-doped catalyst ($MoVO_x$ NCs/CNTs) still outperforms the undoped counterpart (MoO_x NCs/CNTs) in acidic media. $MoVO_x$ NCs/CNTs retain an H_2O_2 selectivity of ~60% over a wide potential window of 0.2–0.6 V (Fig. S11a and b) and exhibit a Tafel slope of 68.5 mV dec^{-1} (Fig. S11c). In addition, negligible performance decay is observed after 2000 accelerated ADT cycles, indicating good cycling stability in acid (Fig. S11d). These results suggest that the V-induced electronic modulation of MoO_x nanoclusters remains operative in acidic media, leading to improved kinetics and H_2O_2 selectivity.

Electronic structures of catalysts

To elucidate the electrocatalysis mechanism of the as-prepared catalysts for the $2e^-$ ORR, it is essential to investigate their electronic structures. Raman spectra showed that the relative intensity of D, G, and D′ bands for CNTs were almost the same (Fig. 3a and c), suggesting negligible changes in nanotube defects after depositing clusters as compared to CNTs.

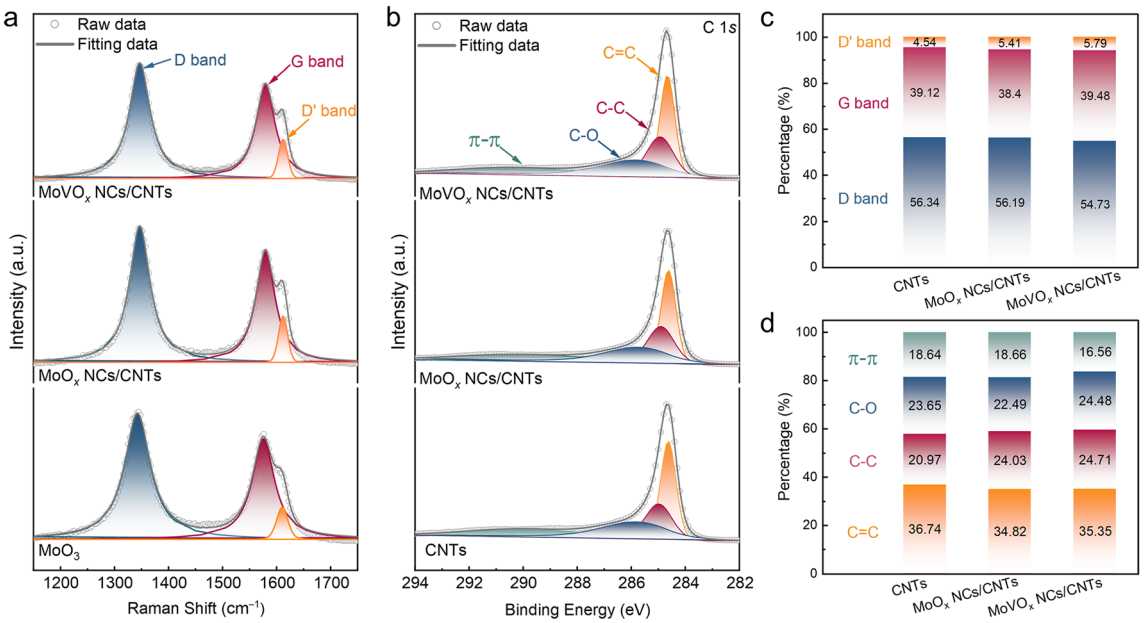

Fig. 3 Characterization of $MoVO_x$ NCs/CNTs. (a) Raman spectra. (b) High-resolution C 1s XPS spectra. The content of different carbon species in CNTs, MoO_x NCs/CNTs and $MoVO_x$ NCs/CNTs determined using Raman (c) and C 1s XPS (d) spectra. The content of species is also shown.

Consistently, the C 1s X-ray photoelectron spectroscopy (XPS) results of $MoVO_x$ NCs/CNTs and MoO_x NCs/CNTs also exhibited similar CNT electronic structures (Fig. 3b, d and S12). These results imply that the synthetic process of nanoclusters did not significantly influence the content of surface oxo-functional groups in CNTs.

The Mo 3d XPS spectra of $MoVO_x$ NCs/CNTs and MoO_x NCs/CNTs reveal a Mo^{5+} spin–orbit doublet at 232.67 and 235.78 eV, which are lower than the peaks of 233.95 and 236.16 eV for Mo^{6+} in the referenced MoO_3 (Fig. 4a).[53] Furthermore, as compared to undoped MoO_x NCs/CNTs, the Mo 3d spectra of $MoVO_x$ NCs/CNTs slightly shift towards lower binding energy, suggesting a lower oxidation state of Mo in $MoVO_x$ NCs/CNT. This observation is further supported by theoretical calculations based on the Mo 3d spectra, where the average oxidation state in MoO_x NCs/CNTs and $MoVO_x$ NCs/CNTs is 5.40 and 5.22 (Fig. S13a), respectively. This phenomenon may be attributed to the doping of V, which modifies the electronic structure of Mo species in $MoVO_x$ NCs/CNTs. Such changes in electron density can optimize the interaction strength between the surface of catalysts and the intermediate of *OOH, facilitating proton-coupled O_2 reduction to *OOH and its following desorption.[54] Meanwhile, based on the O 1s spectra, additional C–O–Mo species were observed in both MoO_x NCs/CNTs and $MoVO_x$ NCs/CNTs (Fig. 4b), indicating the presence of strong interaction between the nanoclusters and CNTs.[55] Furthermore, the introduction of V in $MoVO_x$ NCs/CNTs leads to the generation of more defective O species (Fig. S13b), which could act as additional active sites. This observation may also contribute to the enhanced electrocatalytic activity of $MoVO_x$ NCs/CNTs for the $2e^-$ ORR.

Insights into mechanisms

The surface area and pore structures play crucial roles in determining the performance of electrocatalysts. Normally, a larger surface area and the presence of mesopores could increase the number of exposed electroactive sites and facilitate mass transfer, thus improving the electrocatalytic performance.[4,9,31] We carried out Brunauer–Emmett–Teller (BET) measurements to investigate the surface area and pore features of catalysts. The N_2 adsorption/desorption isotherm curves displayed the typical features of mesoporous materials,[5,56] with BET surface areas of 283.9 $m^2\ g^{-1}$ for MoO_x NCs/CNTs and 286.5 $m^2\ g^{-1}$ for $MoVO_x$ NCs/CNTs, which were larger than that of the blank CNTs (246.5 $m^2\ g^{-1}$), while the pore characteristics of MoO_x NCs/CNTs and $MoVO_x$ NCs/CNTs are similar to those of blank CNTs (Fig. S14a). The content of clusters in CNTs was determined to be ~9 wt% by thermal gravimetric analysis (TGA) (Fig. S14b). These results indicate that loading $MoVO_x$ nanoclusters does not impose a pronounced additional mass-transport limitation. These results imply that the enhanced electrocatalytic activity for the $2e^-$ ORR is mainly attributed to the introduction of nanoclusters into the CNTs.

To gain a deeper understanding of the remarkable performance of the $MoVO_x$ NCs/CNTs, electron energy loss

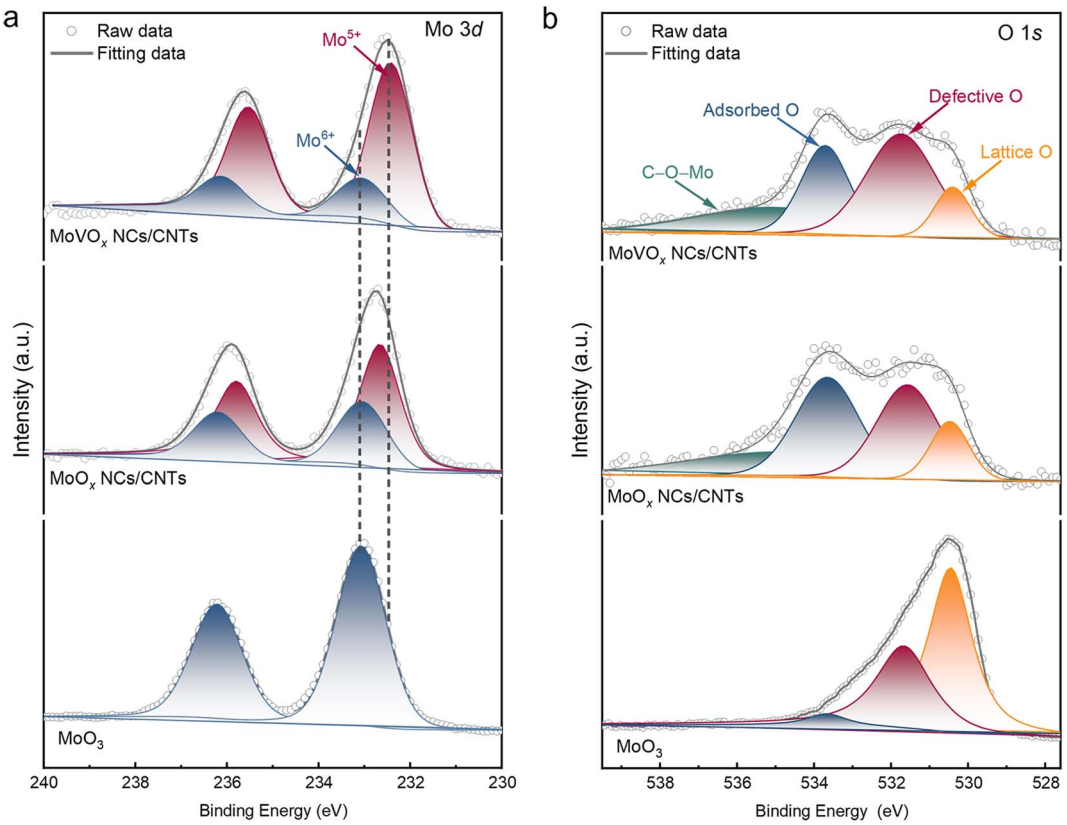

Fig. 4 High-resolution (a) Mo 3d and (b) O 1s XPS spectra of MoO_x NCs/CNTs and $MoVO_x$ NCs/CNTs. MoO_3 is used as a reference.

spectroscopy (EELS) was employed as a powerful tool to unveil the local electronic structures.[57,58] Notably, the region in Fig. 5a corresponds to the blank CNTs segment without nanoclusters, serving as a reference area. In Fig. 5b and c, two regions with typical morphology, where nanoclusters are not only anchored on the outer surface of CNTs but also confined within the cavities of CNTs, were selected. In EELS survey spectra, $MoVO_x$ NCs/CNTs show the existence of V $L_{2,3}$-edge features (510–525 eV) compared to MoO_x NCs/CNTs (Fig. 5d), proving the doping of V atoms in $MoVO_x$ NCs/CNTs, which is consistent with the corresponding EELS mapping (Fig. S15 and S16). The C K-edge EELS spectrum of $MoVO_x$ NCs/CNTs shows an upshift of the carbon energy loss peak (1.1 eV) compared with blank CNTs, while the undoped MoO_x NCs/CNTs show negligible changes (Fig. 5e), indicating that the introduction of V could induce variations in the sp^2 hybridization state of CNTs.[59] It was found that the doping of V reduced the valence state of Mo in $MoVO_x$ NCs/CNTs (Fig. 5f), resulting in higher electronic cloud density at Mo sites,[60] which is consistent with the XPS results (Fig. 4a).

We performed the electron cloud density calculation of MoO_x NCs and $MoVO_x$ NCs to unveil the effect of V doping on the electronic structure of MoO_x NCs (Fig. S17). The calculated electron density distributions reveal higher electron density around Mo in the V-doped structure than in the undoped structure, indicating that V incorporation generates an electron-rich local environment around Mo (Fig. 5g–i). The Gibbs free energy of the key *OOH intermediate was then evaluated on the MoO_x and $MoVO_x$ cluster surfaces. The V doping stabilizes *OOH, lowering $\Delta G_{(*OOH)}$ from 0.85 eV on MoO_x to 0.75 eV on $MoVO_x$ (Fig. S18), indicating that V doping promotes the kinetics of the entire redox process. This modulation is particularly relevant to the $2e^-/4e^-$ pathway competition after *OOH

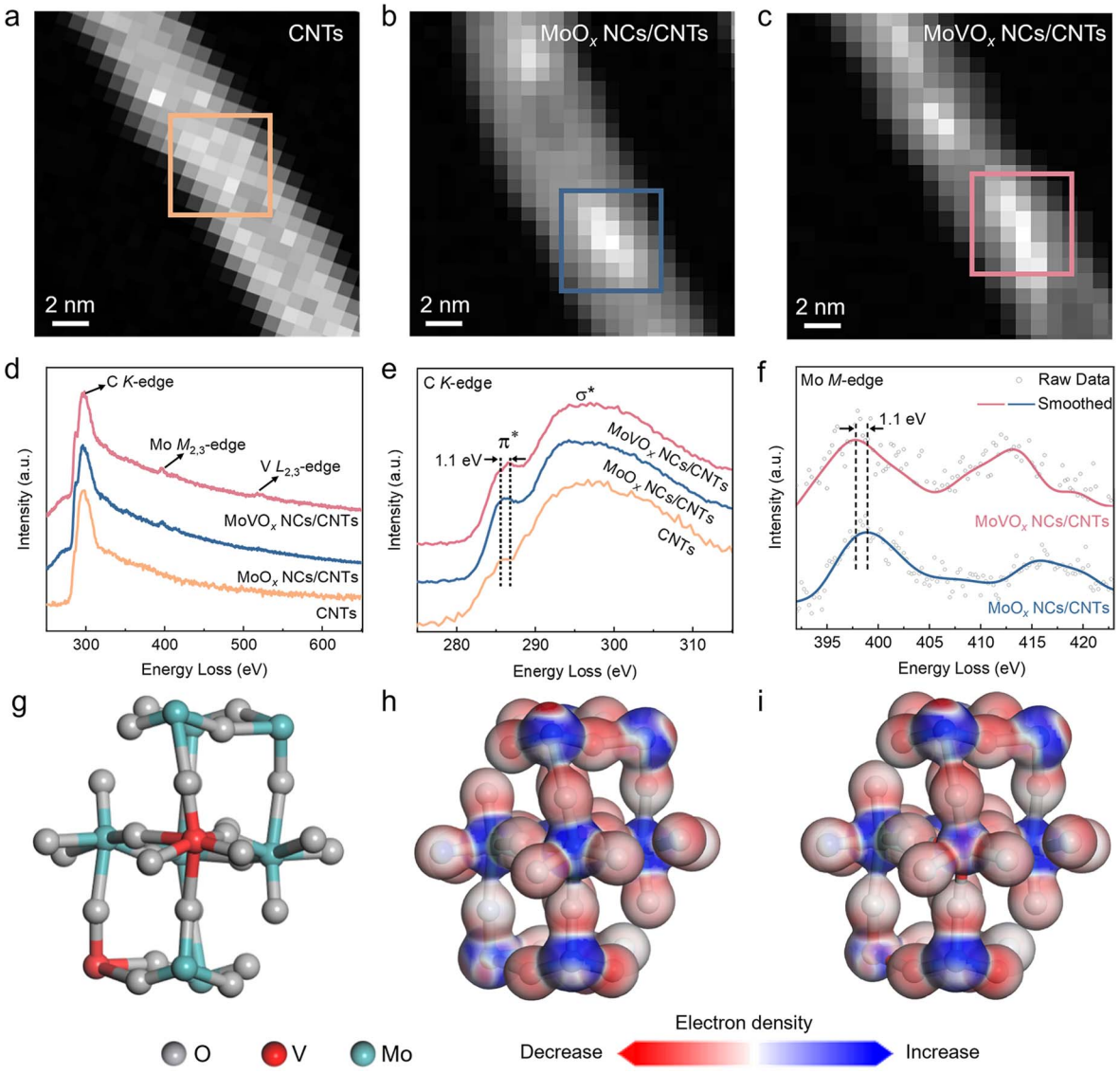

Fig. 5 Insights into mechanisms. STEM-EELS images of CNTs (a), MoO_x NCs/CNTs (b), and $MoVO_x$ NCs/CNTs (c). The EELS survey spectra (d) and C K-edge (e) and Mo M-edge (f) spectra as acquired in the region marked in (a)–(c), respectively. The structural model of MoO_x (g). The calculated distribution of electron density difference of MoO_x (h) and $MoVO_x$ (i).

formation, thereby favouring H_2O_2 formation and enhancing selectivity, while the overall ORR rate (disk current) can remain largely unchanged because it is often governed by O_2 transport and the initial $O_2 \rightarrow$ *OOH activation step. The theoretical calculations corroborate the experimental results obtained from XPS and EELS. The combination of XPS, EELS analysis and the theoretical calculations proved that the doping of V could modify the electronic structure of MoO_x nanoclusters. The modifications of electron density facilitate the enhancement of interaction strength between the surface of catalysts and the *OOH intermediate, thereby facilitating the $2e^-$ ORR process.

Conclusions

Carboxyl functionalized CNTs decorated with V-doped MoO_x nanoclusters ($MoVO_x$ NCs/CNTs) were prepared. Benefitting from the optimized electronic structure modified by V doping, the resulting $MoVO_x$ NCs/CNTs exhibited an impressive H_2O_2 electrosynthesis selectivity of up to 98% at 0.4 V in 0.1 M KOH solution, which far exceeds that of their counterpart MoO_x NCs/CNTs. Importantly, $MoVO_x$ NCs/CNTs could retain more than 93% H_2O_2 electrosynthesis selectivity in a wide potential range from 0.2 V to 0.6 V. Furthermore, $MoVO_x$ NCs/CNTs demonstrated excellent activity stability for 10 h with negligible decay. These excellent results are attributed to the optimization of the electronic structure of $MoVO_x$ NCs/CNTs by V doping, which in turn affects the reaction pathways of the 2-electron and 4-electron reactions. Moreover, the catalyst demonstrates promising activity and stability even in acidic media, confirming the broad applicability of the electronic-structure tuning strategy. The work presents a new perspective on the development of high-performance nanocluster catalysts for the electrocatalysis of O_2 to H_2O_2.

Experimental section

Synthesis of $H_6PMo_9V_3O_{40}$

The synthesis of $H_6PMo_9V_3O_{40}$ follows a methodology similar to that in the previous report but with some modifications.[61] Typically, 2.68 g $Na_2HPO_4 \cdot 7H_2O$ was dissolved in 10 mL of water and mixed with 7.32 g $NaVO_3$ that had been dissolved by heating in 40 mL of water. Subsequently, 1 mL of concentrated H_2SO_4 was introduced into the cooled mixture, yielding a vivid cherry red solution. This solution is then blended with 9.28 g of Na_2MoO_4 dissolved in 30 mL of water. While being vigorously stirred, 17 mL of concentrated H_2SO_4 was gradually incorporated into the mixture. The heated solution was allowed to naturally cool to room temperature. The resultant solution was subjected to 80 mL ethyl ether extraction, with the heteropoly etherate forming the intermediate layer. Upon passing an airstream through the solution, the heteropoly etherate was separated from the ether. Subsequently, rotary evaporation was conducted at 53 °C, resulting in the formation of a distinctive red solid. Following an overnight drying period at 40 °C, the compound was subjected to vacuum recrystallization within an anhydrous calcium chloride environment to further refine its structure.

Synthesis of $MoVO_x$ NCs/CNTs and MoO_x NCs/CNTs

Initially, 50 mg of CNTs were dispersed in 50 mL of DMF through sonication for 30 min. Subsequently, a solution containing 10 mg of $H_6PMo_9V_3O_{40}$ dissolved in 10 mL of DMF was gradually added drop by drop to the CNTs suspension. The resulting mixture underwent an additional 30 min of sonication to ensure thorough mixing. Then, the mixture was stirred at room temperature for a duration of 48 h, and the mixture was subjected to centrifugation, and the resulting precipitate was sequentially washed with DMF, ethanol, and deionized water. The final precipitate was freeze-dried at −60 °C to obtain the precursor powders. For the heat treatment of the precursor powders, a tube furnace was gradually heated to 500 °C under a 10% H_2/Ar atmosphere (100 sccm). Once the temperature reached 500 °C, a quartz boat containing a specific amount of precursor powders was pushed into the center of the tube furnace and maintained for 30 min before being swiftly removed and allowed to cool to room temperature under the protective atmosphere of 10% H_2/Ar. The resultant black powders obtained after this process were identified as $MoVO_x$ NCs/CNTs. The synthesis procedure of MoO_x NCs/CNTs was almost the same as that of $MoVO_x$ NCs/CNTs except for using $H_3PMo_{12}O_{40}$.

Synthesis of deep-oxidized CNTs as a control catalyst

200 mg of CNTs were refluxed in 20 mL of concentrated HNO_3 (68 wt%) at 140 °C for 2.5 h. After the treatment, the solid was collected by centrifugation and dried at 55 °C to obtain the deep-oxidized CNTs product.

Characterization

The HAADF-STEM images were collected by aberration-corrected STEM (FEI Titan Cubed Themis G2) with an X-FEG electron gun and a DCOR aberration corrector operating at 300 kV. STEM-EDX mapping was executed on an FEI Talos F200X electron microscope with a HAADF detector operating at 200 kV. EDX spectra were obtained using a Bruker Super-X detection system. EELS spectra were collected through an aberration-corrected Titan G2 80–300 environmental TEM. It was equipped with a Gatan image filter (Quantum 936) with an energy dispersion of 0.25 eV operated at an acceleration voltage of 300 kV. The zero-loss EELS was acquired immediately after the obtainment of the core-loss EELS on individual nanoparticles. The as-obtained EELS data were further analyzed using a digital micrograph. The position of the core-loss EELS was corrected with the corresponding zero-loss peak followed by subtracting the extrapolated background from the edge of interest. A Fourier-ratio deconvolution was further performed to remove the effect of plural scattering. To facilitate the comparison of diverse spectra, we have normalized the spectra to the most prominent peak of the K-edge of carbon.

Powder X-ray diffraction (XRD) was conducted on a Rigaku SmartLab X-ray diffractometer with Cu-K_α radiation (45 kV, 200 mA, $\lambda = 1.54178$ Å) at a scanning rate of 5° min^{-1} in the 2θ range of 10–80° at room temperature. XPS was performed on a PHI

5000 Versaprobe III photoelectron spectrometer with an Al K_α X-ray source. All peaks were calibrated with the Si 2p peak binding energy at 103.2 eV. The Raman spectra were collected through a Jovin Yvon-Horiba ARAMIS system with a 532 nm laser. The thermogravimetric analysis was conducted through a ZRT-A TGA instrument at a ramp rate of 10 °C min^{-1} from room temperature to 900 °C in air with a dry air flow rate of 30 sccm. Brunauer–Emmett–Teller (BET, 3Flex surface characterization analyzer) analysis was conducted to study the surface area and the porosity distribution of the samples. Fourier transform infrared spectra were recorded on a Thermo Scientific Nicolet iS 50. Inductively coupled plasma mass spectrometry (ICP-MS) was performed on an Agilent 7700.

Electrochemical measurements

All the electrochemical measurements were conducted on an electrochemical workstation (CHI 760E) coupled with a PINE rotating instrument in a standard three-electrode system. A rotating ring disk electrode (RRDE, 5.6 mm in diameter of the disk electrode), a graphite rod, and Ag/AgCl in saturated KCl were employed as the working electrode, counter electrode, and reference electrode, respectively. 0.1 M KOH aqueous solution was used as the electrolyte. All the electrode potential was referenced to the Ag/AgCl reference electrode, which was converted to the reversible hydrogen electrode (RHE) using the equation $E_{(RHE)} = E_{(Ag/AgCl)} + 0.965$ (Fig. S3). The catalyst ink was prepared by dispersing 1 mg active materials in 400 μL solution containing 195 μL isopropanol (IPA), 195 μL DIW, and 10 μL Nafion (5 wt%) solution, followed by ultrasonic treatment for about 60 min.

To detect the ORR activity and H_2O_2 selectivity, linear sweep voltammetry (LSV) measurements were carried out at a scan rate of 5 mV s^{-1} with a catalyst loading of 0.1 mg cm^{-2} under 1600 rpm rotating speed. The scan range is from 0.1 to −0.8 V (*vs.* Ag/AgCl), and the Pt ring potential is set at 1.2 V (*vs.* RHE). Moreover, the working electrode should undergo more than 4 cycles of cyclic voltammetry (CV) at a rate of 100 mV s^{-1} and 4 cycles of CV (scanning rate 20 mV s^{-1}) to stabilize the electrode before the LSV data were recorded. The following equations were used to determine the percent of H_2O_2 and the electron transfer number (n).

$$\%\ (HO_2^-) = 200 \times \frac{I_r/N}{I_d + I_r/N}$$

$$n = 4 \times \frac{I_d/N}{I_d + I_r/N}$$

where I_r means the ring current, I_d means the disk current, and N is the current collection efficiency of the platinum ring.

To understand the ORR stability, LSV measurements were conducted before and after 5000 CV cycles from 0.1 V to −0.8 V (*vs.* Ag/AgCl) at a scanning rate of 100 mV s^{-1}. Chronopotentiometry measurement was also conducted at a constant potential of 0.4 V (*vs.* RHE) with a fixed Pt ring potential of 1.2 V (*vs.* RHE) in 0.1 M KOH and 0.05 M H_2SO_4 under 1600 rpm.

Computational calculations

We employed Castep within Materials Studio 2022 to calculate the electron density difference for MoO_x and V-doped $MoVO_x$. MoO_x and $MoVO_x$ (25% V) nanocluster models were constructed based on the MoO_3 crystal structure (Fig. S17). Within the density functional theory (DFT) framework, the generalized gradient approximation (GGA) with the Perdew–Burke–Ernzerhof (PBE) functional was utilized to approximate the exchange-correlation potential. The calculated energy cutoff was set at 750 eV, with a 5 × 5 × 5 *K*-point mesh for both MoO_x and $MoVO_x$. During structural optimization, the maximum force per atom was required to decrease below 0.05 eV $Å^{-1}$. The energy convergence criterion was set at 2×10^{-5} eV per atom, and the maximum displacement convergence criterion was set at 2×10^{-3} Å.

The Gibbs free energy change can be expressed as

$$\Delta G = \Delta E + \Delta E_{ZPE} - T\Delta S + k_B T \times \ln 10 \times pH$$

where ΔE denotes the total energy difference between reactants and products, obtained *via* density functional theory calculations. ΔE_{ZPE} corresponds to the vibrational frequency of the adsorbed species. ΔS represents the entropy change, with temperature T set at 298.15 K.

Convergence testing of the MoO_3 crystal structure

To ensure the numerical reliability of the computational results, we conducted systematic convergence tests on the truncated energy of plane waves and the *k*-point grid. The tests demonstrated that when the truncated energy reached 750 eV and the *k*-point grid reached 5 × 5 × 5, the total energy variation consistently fell below the convergence criterion of 1 meV per atom (Fig. S19).

Author contributions

F. Y. and J. N. co-supervised the project and led the collaboration efforts. L. Z., Y. L., and F. Y. conceived and designed the experiments. L. Z. and Y. L. performed material synthesis and the characterizations. S. Z. and J. N. performed theoretical calculations. Y. L. wrote the manuscript and L. Z., Y. L., F. Y., S. Z., J. N. revised the manuscript. All authors analysed the data, discussed the results and approved the manuscript.

Conflicts of interest

The authors declare no competing financial interest.

Data availability

All data have been included in the main text and supplementary information (SI). Supplementary information is available. See DOI: https://doi.org/10.1039/d5sc07071f.

Acknowledgements

The authors gratefully acknowledge the Core Research Facilities of Southern University of Science and Technology for characterization. This work was financially supported by the National Natural Science Foundation of China (22475093, 92461307, and 22222504), National Key Research and Development Program of China (2021YFA0717400), Shenzhen Basic Research Project (JCYJ20250604144531041), and State Key Laboratory of Advanced Fiber Materials (Donghua University) (KF2504). Y. B. Li acknowledges the financial support from the Shenzhen Basic Research Project (JCYJ20220530115215035) and China Postdoctoral Science Foundation (2022M711484).

References

1 Y. X. C. Xia, P. Zhu, L. Fan and H. Wang, *Science*, 2019, **366**, 226–231.
2 Y. Xia, X. Zhao, C. Xia, Z. Y. Wu, P. Zhu, J. Y. Kim, X. Bai, G. Gao, Y. Hu, J. Zhong, Y. Liu and H. Wang, *Nat. Commun.*, 2021, **12**, 4255.
3 H. Sheng, E. D. Hermes, X. Yang, D. Ying, A. N. Janes, W. Li, J. R. Schmidt and S. Jin, *ACS Catal.*, 2019, **9**, 8433–8442.
4 P. Cao, X. Quan, X. Nie, K. Zhao, Y. Liu, S. Chen, H. Yu and J. G. Chen, *Nat. Commun.*, 2023, **14**, 172.
5 B. Q. Li, C. X. Zhao, J. N. Liu and Q. Zhang, *Adv. Mater.*, 2019, **31**, 1808173.
6 J. Gao, H. B. Yang, X. Huang, S. F. Hung, W. Cai, C. Jia, S. Miao, H. M. Chen, X. Yang, Y. Huang, T. Zhang and B. Liu, *Chem*, 2020, **6**, 658–674.
7 Y. R. Zheng, S. Hu, X. L. Zhang, H. Ju, Z. Wang, P. J. Tan, R. Wu, F. Y. Gao, T. Zhuang, X. Zheng, J. Zhu, M. R. Gao and S. H. Yu, *Adv. Mater.*, 2022, **34**, 2205414.
8 H. W. Kim, M. B. Ross, N. Kornienko, L. Zhang, J. Guo, P. Yang and B. D. McCloskey, *Nat. Catal.*, 2018, **1**, 282–290.
9 G.-F. Han, F. Li, W. Zou, M. Karamad, J.-P. Jeon, S.-W. Kim, S.-J. Kim, Y. Bu, Z. Fu, Y. Lu, S. Siahrostami and J.-B. Baek, *Nat. Commun.*, 2020, **11**, 2209.
10 M. Wang, N. Zhang, Y. Feng, Z. Hu, Q. Shao and X. Huang, *Angew. Chem., Int. Ed.*, 2020, **59**, 14373–14377.
11 C. Xia, J. Y. Kim and H. Wang, *Nat. Catal.*, 2020, **3**, 605–607.
12 G. Xia, Y. Tian, X. Yin, W. Yuan, X. Wu, Z. Yang, G. Yu, Y. Wang and M. Wu, *Appl. Catal., B*, 2021, **299**, 120655.
13 N. Wang, S. Ma, P. Zuo, J. Duan and B. Hou, *Adv. Sci.*, 2021, **8**, 2100076.
14 J. Tang, T. Zhao, D. Solanki, X. Miao, W. Zhou and S. Hu, *Joule*, 2021, **5**, 1432–1461.
15 Y. Zheng, X. Xu, J. Chen and Q. Wang, *Appl. Catal., B*, 2021, **285**, 119788.
16 Y. J. Sa, J. H. Kim and S. H. Joo, *Angew. Chem., Int. Ed.*, 2019, **58**, 1100–1105.
17 R. Gao, L. Pan, Z. Li, C. Shi, Y. Yao, X. Zhang and J. J. Zou, *Adv. Funct. Mater.*, 2020, **30**, 1910539.
18 K. H. Wu, D. Wang, X. Lu, X. Zhang, Z. Xie, Y. Liu, B. J. Su, J. M. Chen, D. S. Su, W. Qi and S. Guo, *Chem*, 2020, **6**, 1443–1458.
19 Y. Wang, G. I. N. Waterhouse, L. Shang and T. Zhang, *Adv. Energy Mater.*, 2021, **11**, 2003323.
20 S. Siahrostami, S. J. Villegas, A. H. Bagherzadeh Mostaghimi, S. Back, A. B. Farimani, H. Wang, K. A. Persson and J. Montoya, *ACS Catal.*, 2020, **10**, 7495–7511.
21 R. Shen, W. Chen, Q. Peng, S. Lu, L. Zheng, X. Cao, Y. Wang, W. Zhu, J. Zhang, Z. Zhuang, C. Chen, D. Wang and Y. Li, *Chem*, 2019, **5**, 2099–2110.
22 X. Zhang, X. Zhao, P. Zhu, Z. Adler, Z. Y. Wu, Y. Liu and H. Wang, *Nat. Commun.*, 2022, **13**, 2880.
23 Y. Wang, Y. Zhou, Y. Feng and X. Y. Yu, *Adv. Funct. Mater.*, 2022, **32**, 2110734.
24 F. Ma, S. Wang, X. Liang, C. Wang, F. Tong, Z. Wang, P. Wang, Y. Liu, Y. Dai, Z. Zheng and B. Huang, *Appl. Catal., B*, 2020, **279**, 119371.
25 K. Jiang, S. Back, A. J. Akey, C. Xia, Y. Hu, W. Liang, D. Schaak, E. Stavitski, J. K. Nørskov, S. Siahrostami and H. Wang, *Nat. Commun.*, 2019, **10**, 3997.
26 X. Guo, S. Lin, J. Gu, S. Zhang, Z. Chen and S. Huang, *ACS Catal.*, 2019, **9**, 11042–11054.
27 E. Pizzutilo, S. J. Freakley, S. Cherevko, S. Venkatesan, G. J. Hutchings, C. H. Liebscher, G. Dehm and K. J. J. Mayrhofer, *ACS Catal.*, 2017, **7**, 5699–5705.
28 X. Zhao, Q. Yin, X. Mao, C. Cheng, L. Zhang, L. Wang, T. F. Liu, Y. Li and Y. Li, *Nat. Commun.*, 2022, **13**, 2721.
29 L. Han, Y. Sun, S. Li, C. Cheng, C. E. Halbig, P. Feicht, J. L. Hübner, P. Strasser and S. Eigler, *ACS Catal.*, 2019, **9**, 1283–1288.
30 S. Xu, R. Lu, K. Sun, J. Tang, Y. Cen, L. Luo, Z. Wang, S. Tian and X. Sun, *Adv. Sci.*, 2022, **9**, e2201421.
31 D. Iglesias, A. Giuliani, M. Melchionna, S. Marchesan, A. Criado, L. Nasi, M. Bevilacqua, C. Tavagnacco, F. Vizza, M. Prato and P. Fornasiero, *Chem*, 2018, **4**, 106–123.
32 Z. Lu, G. Chen, S. Siahrostami, Z. Chen, K. Liu, J. Xie, L. Liao, T. Wu, D. Lin, Y. Liu, T. F. Jaramillo, J. K. Nørskov and Y. Cui, *Nat. Catal.*, 2018, **1**, 156–162.
33 Y. Sun, L. Silvioli, N. R. Sahraie, W. Ju, J. Li, A. Zitolo, S. Li, A. Bagger, L. Arnarson, X. Wang, T. Moeller, D. Bernsmeier, J. Rossmeisl, F. Jaouen and P. Strasser, *J. Am. Chem. Soc.*, 2019, **141**, 12372–12381.
34 Y. Wang, R. Shi, L. Shang, G. I. N. Waterhouse, J. Zhao, Q. Zhang, L. Gu and T. Zhang, *Angew. Chem., Int. Ed.*, 2020, **59**, 13057–13062.
35 C. Xiao, L. Cheng, Y. Zhu, G. Wang, L. Chen, Y. Wang, R. Chen, Y. Li and C. Li, *Angew. Chem., Int. Ed.*, 2022, **61**, e202206544.
36 Y. Tian, M. Li, Z. Wu, Q. Sun, D. Yuan, B. Johannessen, L. Xu, Y. Wang, Y. Dou, H. Zhao and S. Zhang, *Angew. Chem., Int. Ed.*, 2022, **61**, e202212296.
37 X. Li, S. Tang, S. Dou, H. J. Fan, T. S. Choksi and X. Wang, *Adv. Mater.*, 2022, **34**, e2104891.
38 Y. Jia, Z. Xue, J. Yang, Q. Liu, J. Xian, Y. Zhong, Y. Sun, X. Zhang, Q. Liu, D. Yao and G. Li, *Angew. Chem., Int. Ed.*, 2022, **61**, e202110838.
39 Q. Hu, S. Chen, T. Wagberg, H. Zhou, S. Li, Y. Li, Y. Tan, W. Hu, Y. Ding and X. B. Han, *Angew. Chem., Int. Ed.*, 2023, **62**, e202303290.

40 X. Zhao, F. Wang, X. Kong, R. Fang and Y. Li, *Nat. Commun.*, 2022, **13**, 2591.
41 L. Wang, J. Diao, M. Peng, Y. Chen, X. Cai, Y. Deng, F. Huang, X. Qin, D. Xiao, Z. Jiang, N. Wang, T. Sun, X. Wen, H. Liu and D. Ma, *ACS Catal.*, 2021, **11**, 11469–11477.
42 J. Zhang, M. Wang, T. Wan, H. Shi, A. Lv, W. Xiao and S. Jiao, *Adv. Mater.*, 2022, **34**, e2206960.
43 Y. Wu, Y. Zhao, P. Zhai, C. Wang, J. Gao, L. Sun and J. Hou, *Adv. Mater.*, 2022, **34**, e2202523.
44 S. S. Wang and G. Y. Yang, *Chem. Rev.*, 2015, **115**, 4893–4962.
45 Y. Liu, X. Wu, Z. Li, J. Zhang, S.-X. Liu, S. Liu, L. Gu, L. R. Zheng, J. Li, D. Wang and Y. Li, *Nat. Commun.*, 2021, **12**, 4205.
46 P. Li, X. Duan, Y. Kuang, Y. Li, G. Zhang, W. Liu and X. Sun, *Adv. Energy Mater.*, 2018, **8**, 1703341.
47 T. Zhao, X. Shen, Y. Wang, R. K. Hocking, Y. Li, C. Rong, K. Dastafkan, Z. Su and C. Zhao, *Adv. Funct. Mater.*, 2021, **31**, 2100614.
48 L. Wu, S. Li, L. Li, H. Zhang, L. Tao, X. Geng, H. Yang, W. Zhou, C. Sun, D. Ju and B. An, *Appl. Catal., B*, 2023, **324**, 122250.
49 D. Zhou and B.-H. Han, *Adv. Funct. Mater.*, 2010, **20**, 2717–2722.
50 Q. Chang, P. Zhang, A. H. B. Mostaghimi, X. Zhao, S. R. Denny, J. H. Lee, H. Gao, Y. Zhang, H. L. Xin, S. Siahrostami, J. G. Chen and Z. Chen, *Nat. Commun.*, 2020, **11**, 2178.
51 M. Yang, W. Song, C. Chen, X. Yang, Z. Zhuang, H. Zhang, F. Wang and L. Yu, *Adv. Mater.*, 2025, **37**, 2416401.
52 H. Huang, M. Sun, K. Chen, Y. Che, X. Tang, Z. Li, K. Nie, S. Qian, J. Fang, H. Wang, Y. Wu, Q. Hu, Y. Wang, X. Sun, J. He, Y.-X. Zhang, Z. Zhuang, L. Zhang and Z. Niu, *Angew. Chem., Int. Ed.*, 2025, **64**, e202511844.
53 C. Tang, Y. Jiao, B. Shi, J.-N. Liu, Z. Xie, X. Chen, Q. Zhang and S.-Z. Qiao, *Angew. Chem., Int. Ed.*, 2020, **59**, 9171–9176.
54 F. Xia, B. Li, Y. Liu, Y. Liu, S. Gao, K. Lu, J. Kaelin, R. Wang, T. J. Marks and Y. Cheng, *Adv. Funct. Mater.*, 2021, **31**, 2104716.
55 Y. Yao, Y. Zhu, C. Pan, C. Wang, S. Hu, W. Xiao, X. Chi, Y. Fang, J. Yang, H. Deng, S. Xiao, J. Li, Z. Luo and Y. Guo, *J. Am. Chem. Soc.*, 2021, **143**, 8720–8730.
56 R. Liu, K. Cao, A. H. Clark, P. Lu, M. Anjass, J. Biskupek, U. Kaiser, G. Zhang and C. Streb, *Chem. Sci.*, 2019, **11**, 1043–1051.
57 H. Liu, Y. Zhang, L. Zhang, X. Mu, L. Zhang, S. Zhu, K. Wang, B. Yu, Y. Jiang, J. Zhou and F. Yang, *J. Am. Chem. Soc.*, 2024, **146**, 20193–20204.
58 F. Yang, H. Zhao, W. Wang, L. Wang, L. Zhang, T. Liu, J. Sheng, S. Zhu, D. He, L. Lin, J. He, R. Wang and Y. Li, *Chem. Sci.*, 2021, **12**, 12651–12660.
59 X.-R. Wang, J.-Y. Liu, Z.-W. Liu, W.-C. Wang, J. Luo, X.-P. Han, X.-W. Du, S.-Z. Qiao and J. Yang, *Adv. Mater.*, 2018, **30**, 1800005.
60 C. Cai, M. Wang, S. Han, Q. Wang, Q. Zhang, Y. Zhu, X. Yang, D. Wu, X. Zu, G. E. Sterbinsky, Z. Feng and M. Gu, *ACS Catal.*, 2020, **11**, 123–130.
61 G. A. Tsigdinos and C. J. Hallada, *Inorg. Chem.*, 1968, **7**, 437–441.